



## Mass-transfer-enhanced hydrophobic Bi microsheets for highly efficient electroreduction of CO<sub>2</sub> to pure formate in a wide potential window

Yong Zhang<sup>a</sup>, Rui Zhang<sup>a</sup>, FeiFei Chen<sup>a</sup>, FeiFei Zhang<sup>a</sup>, Yingda Liu<sup>a</sup>, Xiaoya Hao<sup>a</sup>, Haokun Jin<sup>a</sup>, Xinghua Zhang<sup>b</sup>, Zunming Lu<sup>b</sup>, Hong Dong<sup>a</sup>, Feng Lu<sup>a</sup>, Weihua Wang<sup>a</sup>, Hui Liu<sup>c,\*</sup>, Hui Liu<sup>a,\*</sup>, Yahui Cheng<sup>a,\*</sup>

<sup>a</sup> Department of Electronic Science and Engineering and Tianjin Key Laboratory of Process Control and Green Technology for Pharmaceutical Industry, Nankai University, Tianjin 300350, China

<sup>b</sup> School of Material Science and Engineering, Hebei University of Technology, Tianjin 300130, China

<sup>c</sup> Research Group of Quantum-Dot Materials & Devices, Institute of New-Energy Materials, Tianjin University, Tianjin 300350, China



### ARTICLE INFO

**Keywords:**  
Bi microsheets  
CO<sub>2</sub> reduction  
CO<sub>2</sub> mass transfer  
Hydrophobic electrodes  
Solid-state electrolyte

### ABSTRACT

The industrial application of electrochemical CO<sub>2</sub> reduction reaction is challenged by the limited mass transfer and the mixing of products with traditional electrolytes. Here, we propose an in-situ electroreduction strategy to construct hydrophobic Bi microsheets with (012) plane orientation and abundant grain boundaries to solve these problems and maintain high intrinsic activity. The large distance between microsheets and the stable micro-sized hydrophobic structure can trap more air and form smaller solid-liquid interface to stably improve CO<sub>2</sub> mass transfer. The obtained Bi microsheets exhibit high activity and selectivity in a wide potential window. In an H-type cell, the selectivity of formate exceeds 90% over a potential range of -0.8 V to -1.3 V vs. RHE. The pure formate solution is produced using a CO<sub>2</sub> reduction cell with solid-state electrolyte to simplify product separation, and 0.13 M pure formate solution is continuously and stably produced for 110 h at 160 mA cm<sup>-2</sup>.

### 1. Introduction

Electroreduction of carbon dioxide (CO<sub>2</sub>) into fuels and chemical feedstocks is not only one of the ways to address excess CO<sub>2</sub> emissions, but also a potential strategy to achieve carbon-neutral energy cycle [1–4]. As a value-added product of electrochemical CO<sub>2</sub> reduction reaction (ECO<sub>2</sub>RR) [5–7], formate is an important raw material in the chemical industry, a chemical fuel for fuel cells and hydrogen storage [8, 9], and the most economically feasible product in ECO<sub>2</sub>RR [10].

Main group metal elements, including In, Sn, Pb, Bi, etc., show the greatest potential for ECO<sub>2</sub>RR to formate in aqueous electrolytes [11–13]. Among them, Bi has attracted extensive attention because of its unique advantages of rich reserves, non-toxicity, clear active centers and high formate selectivity [8]. Many strategies have been developed to improve the intrinsic activity of Bi-based catalysts and promote CO<sub>2</sub> activation, such as manipulating nanostructures [14,15], doping [16], introducing vacancies [17], exposing specific crystal planes [18,19], building heterojunctions [20,21], and grain boundary engineering [22, 23]. Based on these strategies, the overpotential of ECO<sub>2</sub>RR has been

significantly reduced, and the formate selectivity has reached a high level. However, the high selectivity of formate on most Bi-based electrocatalysts can only be realized at a specific low potential or within a relatively narrow potential range, which is not conducive to the high energy efficiency demand of ECO<sub>2</sub>RR in industrial applications [13]. It is known that the energy-efficient ECO<sub>2</sub>RR in industry requires low overpotential and high selectivity simultaneously, and this high selectivity should be maintained under the commercially favorable high potential/current density (i.e., the partial current density higher than 100 mA cm<sup>-2</sup>) to ensure the high product yields [13]. Unfortunately, limited by the low solubility of CO<sub>2</sub> and the slow mass transfer of CO<sub>2</sub> [24], as the potential (or current density) increases, the localized CO<sub>2</sub> and H<sub>2</sub>O supply on the catalysts surface is unbalanced and favors the hydrogen evolution reaction (HER), which inhibits the formate production.

It is generally believed that hydrophobicity can form a rich solid/liquid/gas three-phase interface, thus enhancing the CO<sub>2</sub> mass transfer and improving the selectivity of ECO<sub>2</sub>RR products at high potentials [24–29]. Polymer coating and constructing rough surface are the most commonly used methods of hydrophobicization [26,28]. The former

\* Corresponding authors.

E-mail addresses: [hui\\_liu@tju.edu.cn](mailto:hui_liu@tju.edu.cn) (H. Liu), [liuhui@nankai.edu.cn](mailto:liuhui@nankai.edu.cn) (H. Liu), [chengyahui@nankai.edu.cn](mailto:chengyahui@nankai.edu.cn) (Y. Cheng).

forms a coating layer on the catalysts surface, which blocks the active sites and weakens the inherent activity of the catalysts [24,26]; the latter often uses small-sized and ultrathin nanosheets to increase roughness and provide sufficient ECO<sub>2</sub>RR active sites [28], but these nanosheets are easily broken into nanoparticles after prolonged ECO<sub>2</sub>RR [30], and the hydrophobic surface cannot be maintained [28], thus resulting in the poor long-term stability. In order to solve these problems, that is, to build a stable hydrophobic surface without blocking the active center and maintaining high intrinsic activity, it is urgent to develop new hydrophobic strategies and hydrophobic catalyst materials.

Compared with nanosheets, microsheets with larger size are stable in structure and not easily broken. Meanwhile, the distance between microsheets is larger than that between nanosheets, which can trap more air and form a smaller solid-liquid contact surface to improve CO<sub>2</sub> mass transfer [31–33]. These characteristics of microsheets provide inspiration for us to construct a novel hydrophobic catalyst. In this work, we propose a Bi-based microsheets ECO<sub>2</sub>RR catalyst with high active plane preferred orientation and a large number of grain boundaries to achieve high formate selectivity in a wide potential window. On the basis of maintaining high hydrophobicity, the preferential orientation of highly active (012) plane of Bi and grain boundaries stabilize the formate intermediate, enhancing the local proton activity on the electrode surface, and thus reducing the free energy barrier for OCHO<sup>-</sup> formation. To realize this special Bi microsheets (Bi MSs) structure, we have developed a simple electroreduction method, which uses (210) plane oriented Bi<sub>4</sub>O<sub>7</sub> microsheets as precursors. As a result, in an H-type electrolytic cell, the Faradaic efficiency of formate (FE<sub>formate</sub>) of Bi MSs is as high as 96.20%, and the potential window is up to wide from –0.8 V to –1.3 V vs. RHE (FE<sub>formate</sub> > 90%). Furthermore, the pure formate solution is produced in a CO<sub>2</sub> reduction cell with solid-state electrolyte (MEA-SSE solid-state electrolytic cell) to reduce the separation cost of downstream products. The Faradaic efficiency of formate exceeds 80% over almost the entire cell pressure range, and 0.13 M pure formate solution is continuously produced with deionized water flow rate of 20 mL h<sup>-1</sup> for 110 h at 160 mA cm<sup>-2</sup>. This work provides a valuable insight for the commercial production of formate by electrochemical reduction of CO<sub>2</sub>.

## 2. Experimental

### 2.1. Synthesis of Bi<sub>4</sub>O<sub>7</sub>

In a typical synthesis, 2.8 g NaBiO<sub>3</sub>·2H<sub>2</sub>O (99%, Macklin) and 2.4 g NaOH (99%, Aladdin) were added to 60 mL deionized water and stirred for 30 min, then the suspension was placed in 100 mL Teflon liner hydrothermal reactor and heated at 180 °C for 18 h. After the reaction, the products were washed with deionized water, ethanol, and dried at 60 °C overnight.

### 2.2. Synthesis of Bi nanoparticles (Bi NPs)

In a typical synthesis, 3.88 g Bi(NO<sub>3</sub>)<sub>3</sub>·5H<sub>2</sub>O (99%, Aladdin) was dissolved in 30 mL ethylene glycol (99%, Aladdin), then the solution was placed in 100 mL Teflon liner hydrothermal reactor and heated at 180 °C for 24 h. After the reaction, the products were washed with deionized water, ethanol, and dried at 60 °C overnight.

### 2.3. Electrochemical test in an H-type electrolytic cell

The electrochemical measurements were performed with an electrochemical workstation (CHI 760E) without iR compensation. The catalysts were made into electrode ink for reducing Bi<sub>4</sub>O<sub>7</sub> to Bi MSs and for CO<sub>2</sub> reduction test. 2 mg Bi<sub>4</sub>O<sub>7</sub> or Bi NPs were ultrasonically dispersed into a solution containing 500 μL isopropanol and 20 μL Nafion to form electrode ink. For CO<sub>2</sub> reduction test, 20 μL electrode ink was dropped onto the L-shaped glassy carbon electrode with a diameter of 5 mm and electroreduced at –1.2 V vs. RHE for 5 min (See Fig. S1 for

a detailed discussion of electroreduction time and potential) to obtain Bi MSs (0.4 mg cm<sup>-2</sup>). For X-ray diffraction (XRD) test, 200 μL electrode ink was dropped onto FTO with an area of 1 cm<sup>-2</sup> and electroreduced at –1.2 V vs. RHE for 10 min to obtain Bi MSs. Bi<sub>4</sub>O<sub>7</sub> reduction and CO<sub>2</sub> reduction tests were performed in a gas-tight three-electrode H-type electrolytic cell using Ag/AgCl (3.0 M KCl) as the reference electrode and Pt mesh as the counter electrode. 20 mL CO<sub>2</sub>-saturated KHCO<sub>3</sub> solution (0.1 M) was used as electrolyte (pH = 6.8), which was stirred at a rate of 500 rpm during ECO<sub>2</sub>RR, and the CO<sub>2</sub> flow rate during ECO<sub>2</sub>RR was maintained at 20 sccm. Convert all potentials measured in the H-cell to the reversible hydrogen electrode (RHE) scale using the following equation:

$$E \text{ (vs. RHE)} = E \text{ (vs. Ag/AgCl)} + 0.197 + 0.0591 \times \text{pH}. \quad (1)$$

The linear sweep voltammetry (LSV) polarization curves were conducted at potentials from 0 V to –1.5 V vs. RHE with a scan rate of 50 mV s<sup>-1</sup>. The double layer capacitance (Cd<sub>d</sub>) of working electrodes were measured by a cyclic voltammetry (CV) test at potentials from 0 V to 0.23 V vs. RHE at various scan rates (20, 40, 60, 80, and 100 mV s<sup>-1</sup>) in 0.1 M Ar-saturated KHCO<sub>3</sub> to compare the electrochemically active surface area (ECSA) of the working electrodes.

The gaseous products of carbon dioxide reduction were analyzed using a gas chromatograph (FULI GC9790 Plus) equipped with thermal conductivity detector (TCD) and flame ionization detector (FID) detectors. Gas chromatography used nitrogen as the carrier gas, and the reduction products were first analyzed for H<sub>2</sub> concentration by TCD and then CO by FID with methanator. Taking CO as an example, the Faradaic efficiency (FE) of gaseous products is calculated as follows [14]:

$$\text{FE}_{\text{CO}} (\%) = \frac{Q_{\text{CO}}}{Q_{\text{tot}}} \times 100\% = \frac{\left( \frac{v}{60 \text{ s/min}} \right) \times \left( \frac{n}{2400 \text{ cm}^3/\text{mol}} \right) \times N \times F \times 100\%}{j}, \quad (2)$$

where  $v$  = 20 sccm is the flow rate of CO<sub>2</sub>,  $n$  is the CO product concentration detected by chromatography and calibrated with standard gas,  $N$  = 2 is the number of electrons required to form a CO molecule,  $F$  is the Faraday constant (96485 C mol<sup>-1</sup>), and  $j$  is the recorded current.

The liquid product was detected by liquid NMR (AVANCE IIITM HD 400 MHz NanoBAY), and 500 μL electrolyzed electrolyte, 100 μL D<sub>2</sub>O, and 10 μL DMSO (0.04 μL mL<sup>-1</sup>) were mixed uniformly in the NMR tube. The formula for calculating the Faradaic efficiency of formate at a given potential is as follows:

$$\text{FE}_{\text{formate}} (\%) = \frac{C_{\text{HCOOH}} \times V \times N \times F \times 100\%}{Q}, \quad (3)$$

where  $C$  is the concentration of formate in the electrolyte,  $V$  is the volume of electrolyte in the cathode cell,  $N$  = 2 is the number of electrons transferred to form formate,  $F$  is the Faraday constant (96485 C mol<sup>-1</sup>), and  $Q$  is the current time integral the amount of charge obtained.

The energy conversion efficiency of CO<sub>2</sub> to formate at a given potential is calculated by the following formula [7]:

$$\Phi_{\text{formate}} = \frac{FE \times \Delta E_{\text{formate}}^0}{\Delta E_{\text{formate}}} \quad (4)$$

In the formula,  $\Phi_{\text{formate}}$  is the energy conversion efficiency,  $FE$  is the Faradaic efficiency of formate,  $\Delta E_{\text{formate}}^0$  is the difference between the standard electrode potential for oxygen production (1.23 V vs. RHE) and the standard electrode potential for CO<sub>2</sub> reduction to formate (–0.2 V vs. RHE),  $\Delta E_{\text{formate}}$  is the difference between the standard electrode potential for oxygen production and the electrode potential on the actual working electrode.

### 2.4. Electrochemical test in a solid-state electrolytic cell

The use of a solid-state electrolyte (SSE) device can avoid the use of

high-concentration electrolyte solutions, thereby simplifying the subsequent separation of liquid products. The composition of the solid-state electrolytic cell from cathode to anode is: cathode metal titanium plate current collector, gas diffusion layer (YLS-30 T, Fuel Cell Store) loaded with Bi MSs catalyst ( $0.4 \text{ mg cm}^{-2}$ ), anion membrane AEM (Sustainion X37–50 Grade 60, SCI Materials Hub), Dowex 50WX8 used as solid H<sup>+</sup> conductor (Sigma), cation membrane CEM (Nafion 115, SCI Materials Hub), Ti mesh loaded with IrO<sub>2</sub>, and anode metal titanium plate current collector. Before the official start of the test, the solid-state electrolytic cell was stabilized for 2 h at a cell voltage of 4.5 V to remove impurities in the SSE and stabilize the current. During the test, a two-electrode body full electrolysis system was used and all voltages reported were full cell voltages without iR compensation. The LSV curves were conducted at potentials from 0 V to – 5 V with scan rate of 50 mV s<sup>-1</sup>. The cathode side was supplied with 20 sccm humidified CO<sub>2</sub> gas, and the anode side was supplied with deionized water for oxygen evolution reaction (OER) to generate H<sup>+</sup>. Deionized water was used to release the produced formate in the solid-state electrolyte at a flow rate of 20 mL h<sup>-1</sup>. The collected pure formate solution was diluted to 40 mL with deionized water for liquid product test.

## 2.5. Characterizations

X-ray diffraction (XRD) patterns were obtained on a powder diffractometer (Rigaku Smart Lab 3 kW) using Cu K $\alpha$  radiation. Scanning electron microscopy (SEM) images of the samples were obtained using a JSM-7800 F scanning electron microscope. Transmission electron microscopy (TEM) and high resolution TEM (HRTEM) images were obtained with a Tecnai G2 F20 TEM operating at 200 kV. X-ray photoelectron spectroscopy (XPS) was performed on a Thermo Scientific ESCALAB 250Xi instrument using a Mg K $\alpha$  X-ray source. The binding energy of the collected spectra was calibrated by the C 1 s binding energy of 284.8 eV. In-situ Raman spectroscopy was recorded on a micro-confocal Raman spectrometer (TEO SR-500I-A) with 532 nm laser. The

ECO<sub>2</sub>RR on Bi MSs electrode was performed in a home-made in-situ Raman cell with a quartz optical window, a Ag/AgCl (3.0 M KCl) reference electrode and a Pt counter electrode. The Raman cell was filled with 0.1 M CO<sub>2</sub>-saturated KHCO<sub>3</sub> electrolyte, and the CO<sub>2</sub> flow rate was maintained at 5 sccm. During the measurement, each potential lasted for 3 min and then each Raman spectroscopy was recorded with twenty accumulations over an acquisition time of 20 s. Atomic force microscope (AFM) images were taken using a Bruker (Dimension Icon) AFM with tapping mode, and the roughness values R<sub>q</sub> are calculated as:

$$R_q = \sqrt{\frac{\sum(Z_i)^2}{N}}, \quad (5)$$

where Z<sub>i</sub> is the current Z value, and N is the number of points within the box cursor. The contact angle was measured by the sessile drop method using JC2000C1 contact angle system at room temperature.

## 3. Results and discussion

### 3.1. Synthesis and Structural Characterizations of Bi<sub>4</sub>O<sub>7</sub>, Bi MSs and Bi NPs

Bi<sub>4</sub>O<sub>7</sub> microsheets were prepared by a facile hydrothermal method. The morphology and structure of the samples are firstly analyzed by SEM. It can be seen that the samples are in the form of microsheets (Fig. S2), which is consistent with TEM image (the inset of Fig. 1b). The XRD pattern (Fig. 1a) matches well with the standard peaks of Bi<sub>4</sub>O<sub>7</sub> (JCPDS No. 04–010–4531) [34]. The main diffraction peaks located at 27.5° and 28.3° can be attributed to the (210) and (102) planes of Bi<sub>4</sub>O<sub>7</sub>, respectively, and the sample has strong (210) plane orientation. In the HRTEM image (Fig. 1b), the (210) plane of Bi<sub>4</sub>O<sub>7</sub> with the lattice fringe spacing of 0.324 nm and the (133) plane of Bi<sub>4</sub>O<sub>7</sub> with the lattice fringe spacing of 0.196 nm can be observed clearly, which further confirms the Bi<sub>4</sub>O<sub>7</sub> phase of the microsheets. The selected area electron diffraction

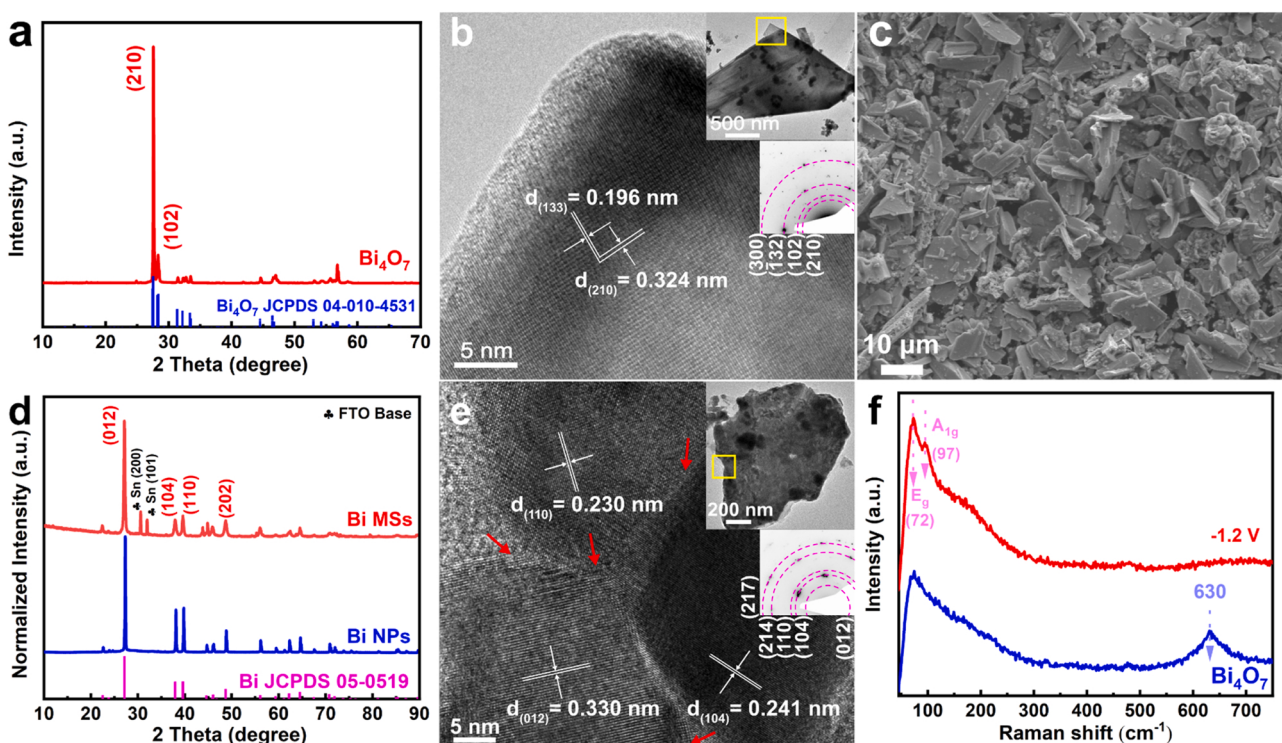


**Fig. 1.** (a) XRD pattern and (b) HRTEM image of Bi<sub>4</sub>O<sub>7</sub>. The inset of (b) shows the TEM image and SAED pattern of Bi<sub>4</sub>O<sub>7</sub>. (c) SEM image of Bi MSs loaded on the electrode. (d) Normalized XRD patterns of Bi MSs and Bi NPs. (e) HRTEM image of Bi MSs. The inset of (e) shows the TEM image and SAED pattern of Bi. (f) In-situ Raman images of Bi<sub>4</sub>O<sub>7</sub> before and after the electroreduction at – 1.2 V vs. RHE.

(SAED) pattern (the inset of Fig. 1b) can also verify the polycrystalline structure of  $\text{Bi}_4\text{O}_7$ . XPS confirms that the surface chemical state of the sample belongs to  $\text{Bi}_4\text{O}_7$  (Fig. S3).

As shown in Fig. S4, Bi MSs were obtained by simple in-situ electroreduction of  $\text{Bi}_4\text{O}_7$  microsheets. Meanwhile, conventional Bi NPs were prepared as controls. Fig. S5 shows a typical CV curve of  $\text{Bi}_4\text{O}_7$  during the electroreduction. A pair of distinct redox peaks can be observed, and there is a large reduction current between  $-0.5$  V and  $0$  V vs. RHE, which corresponds to the reduction of  $\text{Bi}^{3+}$  and  $\text{Bi}^{5+}$  to  $\text{Bi}^0$  in  $\text{Bi}_4\text{O}_7$ . The morphologies of Bi MSs and Bi NPs loaded on the electrode are observed by SEM (Fig. 1c, S6). Bi MSs inherit the microstructure of  $\text{Bi}_4\text{O}_7$  and Bi NPs are nanoparticles, being consistent with the TEM images (the inset of Fig. 1e; Fig. S7). Moreover, the electrode surface of Bi MSs is rougher than that of Bi NPs and the energy dispersive X-ray spectroscopy (EDS) elemental mapping images (Figs. S8, S9) indicate that Bi elements are uniformly distributed on the electrode surface. Fig. 1d shows the normalized XRD patterns of Bi MSs and Bi NPs, respectively. It is observed that the peaks are well indexed to the metal Bi with rhombohedral structure (JCPDS No. 05–0519). It is worth noting that the relative intensity of the (012) peak of the Bi MSs is significantly higher than that of the XRD standard spectrum and the Bi NPs, indicating the oriented growth of the (012) plane of the Bi MSs. It is known that the Bi atomic arrangement on the  $\text{Bi}_4\text{O}_7$  (210) crystal plane has a parallelogram structure unit similar to that on the metal Bi (012) crystal plane. Therefore, the rearrangement of Bi atoms from the (210) plane of  $\text{Bi}_4\text{O}_7$  to the (012) plane of Bi is the most popular and reasonable in thermodynamics. Moreover, the preferential orientation of highly active (012) plane of Bi may promote the formation and stabilization of key intermediates during the ECO<sub>2</sub>RR process [18,19]. SAED pattern of the Bi MSs (the inset of Fig. 1e) confirms the phase of Bi. It is observed that multiple diffraction spots appear on some planes, such as (012), (104), (110), (214) and (217) planes, proving the polycrystalline structure of the sample. HRTEM images of Bi MSs (Fig. 1e, S10a) exhibit grains with different lattice orientations, and the grain boundaries (GBs) can be observed and indicated by red arrows. In contrast, no GBs are observed

in Bi NPs (Fig. S10b). The construction of GBs is a powerful strategy to enhance the catalytic performance, i. e., intrinsic activity and selectivity in ECO<sub>2</sub>RR [22,23,35,36].

The evolution of structure and chemical state of  $\text{Bi}_4\text{O}_7$  in the process of electroreduction to Bi is further observed by in-situ Raman spectroscopy (Fig. 1f).  $\text{Bi}_4\text{O}_7$  peak is observed at  $630 \text{ cm}^{-1}$ , being consistent with the previously reports [37]. After in-situ reduction, the Raman peaks of Bi MSs at  $72 \text{ cm}^{-1}$  and  $97 \text{ cm}^{-1}$  are observed, corresponding to the  $E_g$  and  $A_{1g}$  vibrational modes of the Bi-Bi bond in metal Bi respectively [38], and no oxidation peaks are observed. Moreover, XPS spectra of Bi MSs and Bi NPs (Fig. S11) also exhibit metallic Bi peaks.

### 3.2. ECO<sub>2</sub>RR performance in an H-type electrolytic cell

The LSV curves of Bi MSs and Bi NPs in  $0.1 \text{ M CO}_2$ -saturated  $\text{KHCO}_3$  solution are shown in Fig. 2a. LSV curves exhibit a cathodic current onset at approximately  $-0.7$  V vs. RHE due to ECO<sub>2</sub>RR, and beyond that, the current density of Bi MSs increases faster and reaches  $-15.31 \text{ mA cm}^{-2}$  at  $-1.5$  V vs. RHE, indicating that Bi MSs have higher activity in the ECO<sub>2</sub>RR process. The Nyquist plot (Fig. S12) shows that the electron transport rate on Bi MSs is much faster than that on Bi NPs, which is consistent with the results of LSV.

ECO<sub>2</sub>RR tests were performed within the potential range of  $-0.7$  V to  $-1.5$  V vs. RHE using the potentiostatic method (Fig. S13). The  $^1\text{H}$  NMR spectrum (Fig. S14) confirms that formate is the only liquid product. Fig. 2b shows the  $\text{FE}_{\text{formate}}$  of Bi MSs and Bi NPs, respectively. The  $\text{FE}_{\text{formate}}$  of Bi MSs is higher than that of Bi NPs at all applied potentials. Specifically, Bi MSs exhibit the  $\text{FE}_{\text{formate}}$  of more than 90% under a wide potential window (from  $-0.8$  V to  $-1.3$  V vs. RHE) and exhibit the highest  $\text{FE}_{\text{formate}}$  of 96.2% at  $-1.0$  V vs. RHE. As shown in Fig. 2c, compared with the previously reported Bi-based electrocatalysts [7,9,17–20,23,28,39,40], Bi MSs show the advantage in potential window range (500 mV) with high Faradaic efficiencies (Table S1). For Bi MSs and Bi NPs,  $\text{H}_2$  and CO are the main gas products and the main competitors of formate (Fig. S15). Compared with Bi NPs, the  $\text{H}_2$

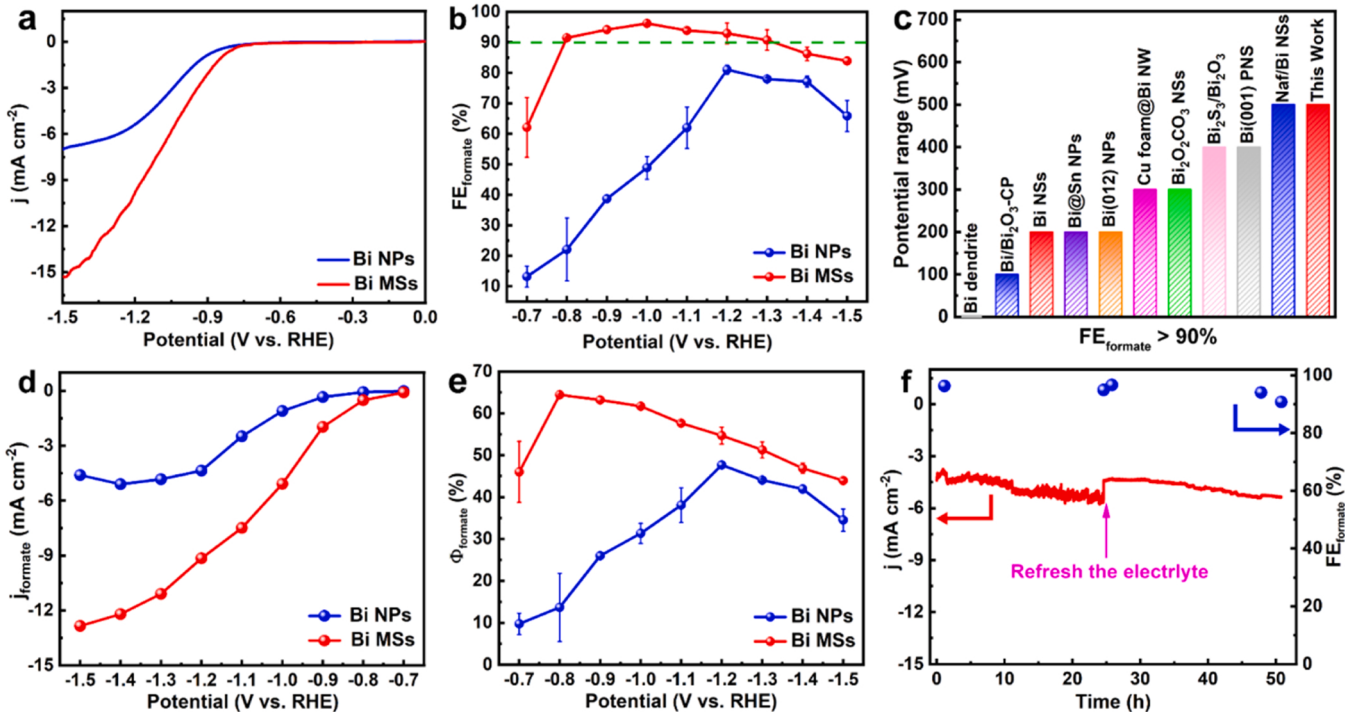


**Fig. 2.** (a) LSV curves of Bi NPs and Bi MSs in  $0.1 \text{ M CO}_2$ -saturated  $\text{KHCO}_3$  solution ( $50 \text{ mV s}^{-1}$ ). (b)  $\text{FE}_{\text{formate}}$  of Bi NPs and Bi MSs at different applied potentials, respectively. (c) Comparison of the potential range corresponding to the  $\text{FE}_{\text{formate}} > 90\%$  of the Bi MSs in this work with other advanced Bi-based catalysts. (d)  $j_{\text{formate}}$  and (e)  $\Phi_{\text{formate}}$  of Bi NPs and Bi MSs. (f) Long-term stability test of Bi MSs at  $-1.0$  V vs. RHE.

produced by using Bi MSs is greatly suppressed to less than 10% under a wide potential window (from  $-0.8$  to  $-1.3$  V vs. RHE). The activity of the catalysts to produce formate were further evaluated by the partial current density of formate ( $j_{\text{formate}}$ ). Bi MSs have higher  $j_{\text{formate}}$  than Bi NPs at all applied potentials (Fig. 2d). At  $-1.0$  V and  $-1.3$  V vs. RHE, the  $j_{\text{formate}}$  of Bi MSs is  $-5.08 \text{ mA cm}^{-2}$  and  $-11.10 \text{ mA cm}^{-2}$ , which is 4.62 and 2.30 times that of Bi NPs, respectively. The energy conversion efficiency (Formula 4) of Bi MSs for formate ( $\Phi_{\text{formate}}$ ) exceeds 50% in a wide potential window of  $-0.8$  V to  $-1.3$  V vs. RHE (Fig. 2e). Compared with other reported Bi-based catalysts [7], the Bi MSs exhibit higher  $\text{CO}_2$  to formate conversion efficiency (64.23%).

The durability of a catalyst is crucial for practical applications. During a long-term  $\text{ECO}_2\text{RR}$ , the durability of Bi MSs was evaluated by testing the current density and Faradaic efficiency at  $-1.0$  V vs. RHE (Fig. 2f). Apparently, the Bi MSs demonstrate an outstanding stability over 52 h. Although the current density increases slightly due to the accumulation of  $\text{HCOO}^-$  in the electrolyte, it can be quickly recovered when the electrolyte is refreshed, and the  $\text{FE}_{\text{formate}}$  (with a minimum of 90.8%) is always higher than 90%. SEM was used to study the morphological evolution of Bi MSs before and after electrolysis (Fig. S16). The morphology of Bi MSs remains unchanged, maintaining

their robust microsheets structure. All these results verify the good stability of Bi MSs for  $\text{ECO}_2\text{RR}$  and outperform other Bi-based catalysts that have been reported (Table S2). In summary, Bi MSs show significant suppression for  $\text{H}_2$  formation relative to Bi NPs, with  $\text{FE}_{\text{formate}}$  of more than 90% under a wide potential window and maintain long-term stability during  $\text{ECO}_2\text{RR}$ .

### 3.3. Mechanism analysis

To better understand the enhanced electrocatalytic performance of Bi MSs, the  $\text{ECO}_2\text{RR}$  mechanism of the as-prepared Bi MSs electrocatalyst were systematically investigated. Firstly, the Cdl was measured to rule out the ECSA effect (Figs. S17, S18). The Cdl values of Bi MSs and Bi NPs are  $0.62 \text{ mF cm}^{-2}$  and  $0.30 \text{ mF cm}^{-2}$ , respectively. These Cdl values were used to normalize the  $j_{\text{formate}}$  of Bi MSs and Bi NPs (Fig. S19) and the normalized  $j_{\text{formate}}$  of Bi MSs is still higher than that of Bi NPs at various test potentials, which indicates that the intrinsic activity of Bi MSs is higher than that of Bi NPs.

To further investigate the reasons for the superior performance of Bi MSs, in-situ Raman spectroscopy was used to monitor the evolution of reaction intermediates on the catalyst surface to reveal the  $\text{ECO}_2\text{RR}$

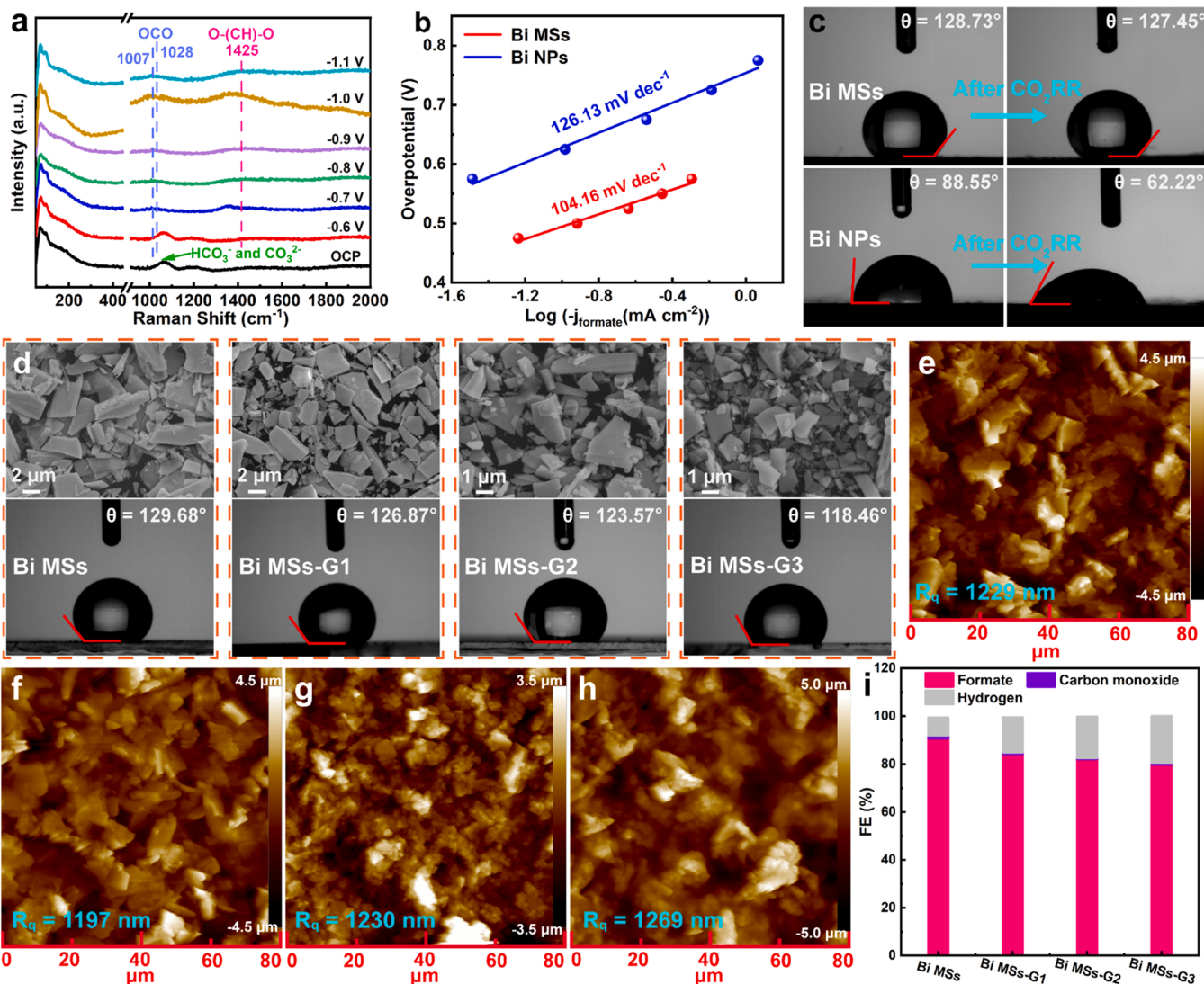


**Fig. 3.** (a) In-situ Raman spectra of Bi MSs  $\text{ECO}_2\text{RR}$  at open circuit potential (OCP) and from  $-0.6$  V to  $-1.1$  V vs. RHE. (b) Tafel slopes of Bi MSs and Bi NPs. (c) Contact angles of Bi MSs and Bi NPs before and after  $\text{ECO}_2\text{RR}$  reaction. (d) Changes in morphology and corresponding contact angles of Bi MSs, Bi MSs-G1, Bi MSs-G2 and Bi MSs-G3. (e-h) AFM images of (e) Bi MSs, (f) Bi MSs-G1, (g) Bi MSs-G2 and (h) Bi MSs-G3. (i) Changes in FEs of Bi MSs, Bi MSs-G1, Bi MSs-G2 and Bi MSs-G3 at  $-1.3$  V vs. RHE.

process (Fig. 3a). The Raman signal at  $1007\text{ cm}^{-1}$  and  $1028\text{ cm}^{-1}$  is the vibration of O-C-O, and the Raman signal at  $1425\text{ cm}^{-1}$  is the vibration of O-(CH)-O. Both O-C-O and O-(CH)-O are key intermediates in formate production [41–43]. Moreover, according to the density functional theory (DFT) calculation [18], the adsorption of  $\text{CO}_2$  with Bi-O coordination to form \*OCHO intermediate is the most favorable in terms of reaction free energy, and the (012) plane can effectively stabilize \*OCHO intermediate to enhance  $\text{ECO}_2\text{RR}$  activity. Reaction intermediates and thermodynamically optimal reaction path indicate that  $\text{ECO}_2\text{RR}$  on metallic Bi may follow a reaction pathway of  $\text{CO}_2^- \rightarrow \text{OCHO}^- \rightarrow \text{HCOO}^-$ , as shown in Eqs. 6–9 [40], and compete with the HER (Eq. 10):



During  $\text{ECO}_2\text{RR}$ ,  $\text{CO}_2$  molecule is firstly adsorbed on the surface of metallic Bi (Eq. 6) which is mainly controlled by the mass transfer of  $\text{CO}_2$  on the electrode surface; subsequently,  $\text{CO}_2$  is activated by capturing one electron to form  $\text{CO}_2^-$  species (Eq. 7) and the reduction of  $\text{CO}_2^-$  species is achieved by capturing proton from  $\text{HCO}_3^-$  to generate  $\text{OCHO}^-$  (Eq. 8), which is mainly controlled by the intrinsic activity of the catalyst; finally,  $\text{OCHO}^-$  desorbs to form  $\text{HCOO}^-$  (Eq. 9). Based on this, it has been reported that the  $\text{ECO}_2\text{RR}$  activity of the catalyst is mainly controlled by the intrinsic activity of the catalyst at low potentials, and the mass transfer of  $\text{CO}_2$  at high potentials [35]. Therefore, the intrinsic activity and  $\text{CO}_2$  mass transfer capacity of the catalysts are investigated separately.

The  $\text{ECO}_2\text{RR}$  kinetics and rate-determining step (RDS) of the catalysts were examined by the Tafel slope (Fig. 3b). The Tafel slope of Bi MSs is  $104.16\text{ mV dec}^{-1}$ , which is lower than that of Bi NPs ( $126.13\text{ mV dec}^{-1}$ ), indicating that the  $\text{ECO}_2\text{RR}$  kinetics of Bi MSs is faster. The Tafel slopes of both Bi MSs and Bi NPs are close to  $118\text{ mV dec}^{-1}$ , indicating that  $\text{CO}_2$  activation (Eq. 6) is the RDS [20]. The  $\text{CO}_2$  activation process can be further understood by studying the adsorption strength of  $\text{CO}_2^-$  intermediates on the catalysts. In  $0.1\text{ M N}_2\text{-saturated NaOH solution}$ ,  $\text{OH}^-$  was used instead of  $\text{CO}_2^-$  for oxidative LSV scans (Fig. S20). The adsorption potential of Bi MSs to surface  $\text{OH}^-$  is lower than that of Bi NPs, indicating that Bi MSs possessed stronger adsorption affinity of  $\text{OH}^-$ , and hence Bi MSs could efficiently stabilize the  $\text{CO}_2$  intermediate [5]. The isotope labeling method (Fig. S21a) shows that the protons in formate are mainly derived from  $\text{HCO}_3^-$ , and hence the performance of  $\text{ECO}_2\text{RR}$  was tested in different concentrations of  $\text{KHCO}_3$  solution to explore the local proton activity of the catalysts [28]. Bi MSs exhibited higher  $\text{FE}_{\text{formate}}$  than Bi NPs over the entire  $\text{HCO}_3^-$  concentration range (Fig. S21b),  $\text{FE}_{\text{formate}}$  of Bi MSs did not increase with increasing  $\text{HCO}_3^-$  concentration, whereas that of Bi NPs increased with increasing  $\text{HCO}_3^-$  concentration (from 48.85% in  $0.1\text{ M HCO}_3^-$  to 71.86% in  $1.0\text{ M HCO}_3^-$ ). This indicates that the local proton activity of Bi MSs has reached the optimum at low concentration of  $\text{HCO}_3^-$ . The above results indicate that Bi MSs can efficiently stabilize the formate intermediate and form  $\text{OCHO}^-$ , that is, Bi MSs have higher intrinsic activity, which improves the selectivity of formate at low potentials.

As the main factor affecting the activity of  $\text{ECO}_2\text{RR}$  at high potential,  $\text{CO}_2$  mass transfer was further investigated. Recent studies have claimed that the hydrophobic catalyst surface is conducive to the formation of abundant gas-liquid-solid three-phase interfaces, which can effectively enhance the  $\text{CO}_2$  mass transfer on the catalyst surface [26–28]. In order to verify the wettability of the electrode, the catalysts were loaded on a glassy carbon electrode and the contact angle was measured (Fig. 3c,

S22). The contact angle of Bi MSs is  $128.73^\circ$ , showing hydrophobicity. In contrast, the contact angle of Bi NPs is  $88.55^\circ$ , showing hydrophilicity. Interestingly, the contact angle of Bi NPs decreases to  $62.22^\circ$  after one hour of  $\text{ECO}_2\text{RR}$  test. This indicates that Bi NPs are easily submerged during the  $\text{ECO}_2\text{RR}$  process. However, after  $\text{ECO}_2\text{RR}$ , the contact angle of Bi MSs remains almost unchanged with a value of  $127.45^\circ$ , indicating that Bi MSs maintain the electrode hydrophobicity during the reaction.

To explain why the microsheets structure has good hydrophobicity and the mechanism that microsheets structure can promote  $\text{ECO}_2\text{RR}$ , Bi MSs were ground and broken to reduce the size of the sheets, and the grinding time was controlled to 1 min, 2 min and 3 min as three sets of comparative samples, named as Bi MSs-G1, Bi MSs-G2 and Bi MSs-G3, respectively. Fig. 3d shows the changes in morphology and contact angle of Bi MSs with increasing grinding time. SEM images indicate that with the increase of grinding time, the size of the microsheets gradually decreases and finally turn into nanosheets. The average sheets lengths (Fig. S23) of Bi MSs, Bi MSs-G1, Bi MSs-G2 and Bi MSs-G3 are  $4.6 \pm 0.1\text{ }\mu\text{m}$ ,  $1.9 \pm 0.1\text{ }\mu\text{m}$ ,  $1.09 \pm 0.02\text{ }\mu\text{m}$  and  $0.73 \pm 0.01\text{ }\mu\text{m}$ , respectively. Four sets of catalysts were uniformly loaded on FTO ( $0.4\text{ mg cm}^{-2}$ ) for contact angle and AFM tests. The contact angle of the samples gradually decreases with the increase of grinding time and finally the contact angle of Bi MSs-G3 was reduced to  $118.46^\circ$ , indicating that the reduction of the sheets size reduces the hydrophobicity of the catalysts. Based on the AFM images (Fig. 3e-h), the roughness  $R_q$  of the Bi MSs, Bi MSs-G1, Bi MSs-G2 and Bi MSs-G3 surface are calculated to be  $1229\text{ nm}$ ,  $1197\text{ nm}$ ,  $1230\text{ nm}$  and  $1269\text{ nm}$ , respectively, which indicates that the roughness of the catalysts on the electrode surface hardly changes with the decrease of the sheets size. According to the Wenzel model, the roughness enhances the hydrophobicity when the electrode surface is in full contact with water. However, in this work, without changing the electrode surface roughness, the contact angle of the electrode surface decreases with decreasing size. Hence, it must be considered that the catalyst is not in complete contact with water, that is, the sheets structure can trap air and form a three-phase interface. Here the relationship between sheets size and contact angle  $\theta$  is explored using the Cassie-Baxter model [33]:

$$\cos\theta = f(\cos\theta_Y + 1) - 1, \quad (11)$$

where  $f$  is the liquid-solid contact fraction and  $\theta_Y$  is the Young's contact angle ( $\theta_Y$  is related to the chemical state of the material surface). Considering that the catalysts surfaces are all wrapped by Nafion, it can be approximated that the chemical state ( $\theta_Y$ ) of the electrode surface is the same, and the contact angle is only related to  $f$  value. The reported results [31–33] show that increasing the micro-nanostructure spacing can reduce the  $f$  value, which in turn increases the contact angle. Compared with nanosheets, the microsheets have a larger spacing and a smaller solid-liquid contact area, so the microsheets exhibit better hydrophobicity than nanosheets. Moreover, the decrease in the contact angle of Bi MSs-G3 before and after the long-term reaction further reflects the stability advantage of microsheets compared with nanosheets (Fig. S24). The LSV curves of post-grinding Bi MSs in  $0.1\text{ M CO}_2\text{-saturated KHCO}_3$  solution (Fig. S25) show that their current densities are the same as that of Bi MSs at low potentials. This indicates that the intrinsic activity of the catalysts is not changed by grinding, and thus the activity of the catalysts for  $\text{ECO}_2\text{RR}$  at low potentials is not changed. However, at high potentials, such as  $-1.3\text{ V vs. RHE}$ , Bi MSs-G1, Bi MSs-G2 and Bi MSs-G3 have relatively low current densities of  $-11.64$ ,  $-10.17$  and  $-9.21\text{ mA cm}^{-2}$  compared with that of Bi MSs ( $-12.22\text{ mA cm}^{-2}$ ). Moreover, due to the decrease of hydrophobicity, the electrode surface is in contact with more electrolyte, resulting in an increase in the  $\text{FE}$  of  $\text{H}_2$  (Fig. 3i) and a decrease in  $\text{FE}_{\text{formate}}$ . For example, the  $\text{FE}_{\text{formate}}$  of Bi MSs-G3 is reduced to 79.84%, much lower than that of Bi MSs (90.73%). These are because that due to the decrease in hydrophobicity, the three-phase interface is reduced and less  $\text{CO}_2$  is captured on the

electrode surface, which reduces the activity of the catalyst at high potentials for ECO<sub>2</sub>RR. The above results suggest that due to the appropriate spacing between the microsheets, a stable hydrophobic surface can be constructed, forming abundant three-phase interface. It facilitates the CO<sub>2</sub> mass transfer on the electrode surface, and hence enhances the activity of Bi MSs at high potentials.

Based on all the analysis above, Fig. 4 presents an explanation of the excellent activity of Bi MSs. It shows that Bi NPs are hydrophilic (Fig. 4a), while Bi MSs are hydrophobic (Fig. 4b). At low potential, benefiting from the preferential orientation of the highly active (012) plane and a large number of grain boundaries, Bi MSs have excellent intrinsic activity, the formate intermediates are stabilized and the free energy barrier in the formation of OCHO<sup>-</sup> is reduced, thereby improving the selectivity of formate. At high potentials, the kinetics of CO<sub>2</sub>RR and competitive HER increase rapidly. Therefore, the mass transfer of CO<sub>2</sub> becomes the key to control the selectivity of formate. As shown in Fig. 4c, the hydrophilic Bi NPs electrode have abundant liquid-solid interfaces, so H<sup>+</sup> in solution has more opportunities to interact with electrons to generate H<sub>2</sub>. In contrast, the hydrophobic Bi microsheets electrode surface has rich three-phase interfaces (Fig. 4d) with more CO<sub>2</sub> molecules in the gas phase, so the local concentration of CO<sub>2</sub> increases. The diffusion of these concentrated CO<sub>2</sub> into the electrolyte enhances the mass transfer of CO<sub>2</sub> from the electrolyte to the catalyst surface, thus improving the selectivity of Bi MSs for formate production and inhibiting HER.

#### 3.4. ECO<sub>2</sub>RR performance in a solid-state electrolytic cell

In addition to the issues of selectivity and activity, the production of formate by ECO<sub>2</sub>RR also encounters the problem of mixing products with electrolytes (such as KHCO<sub>3</sub>, KOH, etc.), requiring energy-intensive downstream separation and increasing the cost of formate [22]. Using a solid-state electrolytic cell to produce pure formate solution can effectively solve the above problems [5,6,22,30]. The schematic diagrams and physical photos of the solid-state electrolytic cell are shown in Fig. 5a and S26, respectively. On the anode side, IrO<sub>2</sub>/Ti mesh was selected as the catalyst for oxygen evolution reaction, and H<sup>+</sup> was

released in water to combine with HCOO<sup>-</sup> in solid-state electrolyte (SSE) (Fig. 5b). The SEE adopted Dowex 50WX8H<sup>+</sup> type with particle size of 50 μm (Fig. S27). The cathode catalyst was YLS-30 T gas diffusion layer (GDL) supported with Bi MSs (with electrode geometric area of 1 cm<sup>2</sup>). SEM shows that the catalyst is uniformly distributed on the GDL (Fig. S28). The LSV curves of Bi MSs and Bi NPs in a solid-state electrolytic cell at a flow rate of 20 mL h<sup>-1</sup> of deionized water are shown in Fig. 5c. LSV curves exhibit a cathodic current onset at approximately 2.0 V due to ECO<sub>2</sub>RR, and beyond that, the current density of Bi MSs increases faster and reaches 100 mA cm<sup>-2</sup> at 4.5 V, which is the commercially favorable current density. The FE<sub>formate</sub> of Bi MSs remains higher than 80% in almost the entire cell voltage range (Fig. 5d), and the FE<sub>formate</sub> reaches the maximum value of 85.8% at 4.5 V with the partial current density of 137.3 mA cm<sup>-2</sup> (Fig. S29). By slowing down the deionized water flow to 10 mL h<sup>-1</sup>, a higher formate concentration of 0.2 M is achieved with an FE of 64.0% (Fig. S30). Obviously, although reducing the flow rate achieves higher formate concentration, the accumulation of product reduces the energy utilization efficiency, so 20 mL h<sup>-1</sup> is a suitable flow rate of deionized water. As a result, 0.13 M pure formate solution is continuously produced with the flow rate of 20 mL h<sup>-1</sup> by the solid-state electrolytic cell. The pH of the resulting formate solution is about 2.33 (Fig. S31), which is in good agreement with the theoretical pH of 2.32 of 0.13 M formate solution. <sup>1</sup>H NMR (Fig. 5e) and <sup>13</sup>C NMR (Fig. S32) verify the high purity of the formate solution. Finally, the formate solution is continuously produced for 110 h at a constant current density of 160 mA cm<sup>-2</sup> (Fig. 5f). More excitingly, during the long-term ECO<sub>2</sub>RR test, the cell voltage shows negligible change. The FE<sub>formate</sub> is maintained above 80%, and a total of 2.1 L of pure formate solution with a concentration of 0.13 M is produced (Fig. S33). The SEM image and contact angle of Bi MSs loaded on GDL after stability test further confirm the good stability of Bi MSs for ECO<sub>2</sub>RR (Fig. S34). Moreover, hydrophobicity of the electrode surface can still improve the ECO<sub>2</sub>RR performance of the catalyst in the solid-state electrolysis cell. The FE<sub>formate</sub> of Bi MSs is higher than that of Bi NPs (Fig. S35) in the entire cell voltage range, especially at high cell voltage. For example, at the cell voltage of 5.0 V, the FE<sub>formate</sub> of Bi MSs is 84.5%, which is much higher than that of Bi NPs (53.1%). Bi MSs

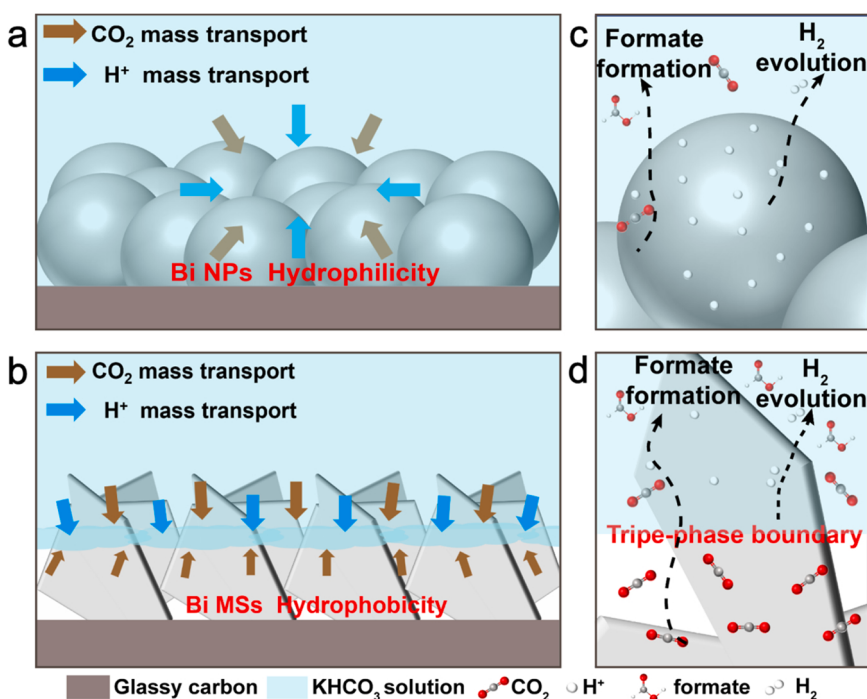


**Fig. 4.** (a) CO<sub>2</sub> and H<sup>+</sup> mass transport at the liquid-solid interface of Bi NPs, (b) gas-solid-liquid interface of Bi MSs. Schematic diagram of the generation of formate and hydrogen on the surface of (c) Bi NPs, (d) Bi MSs.

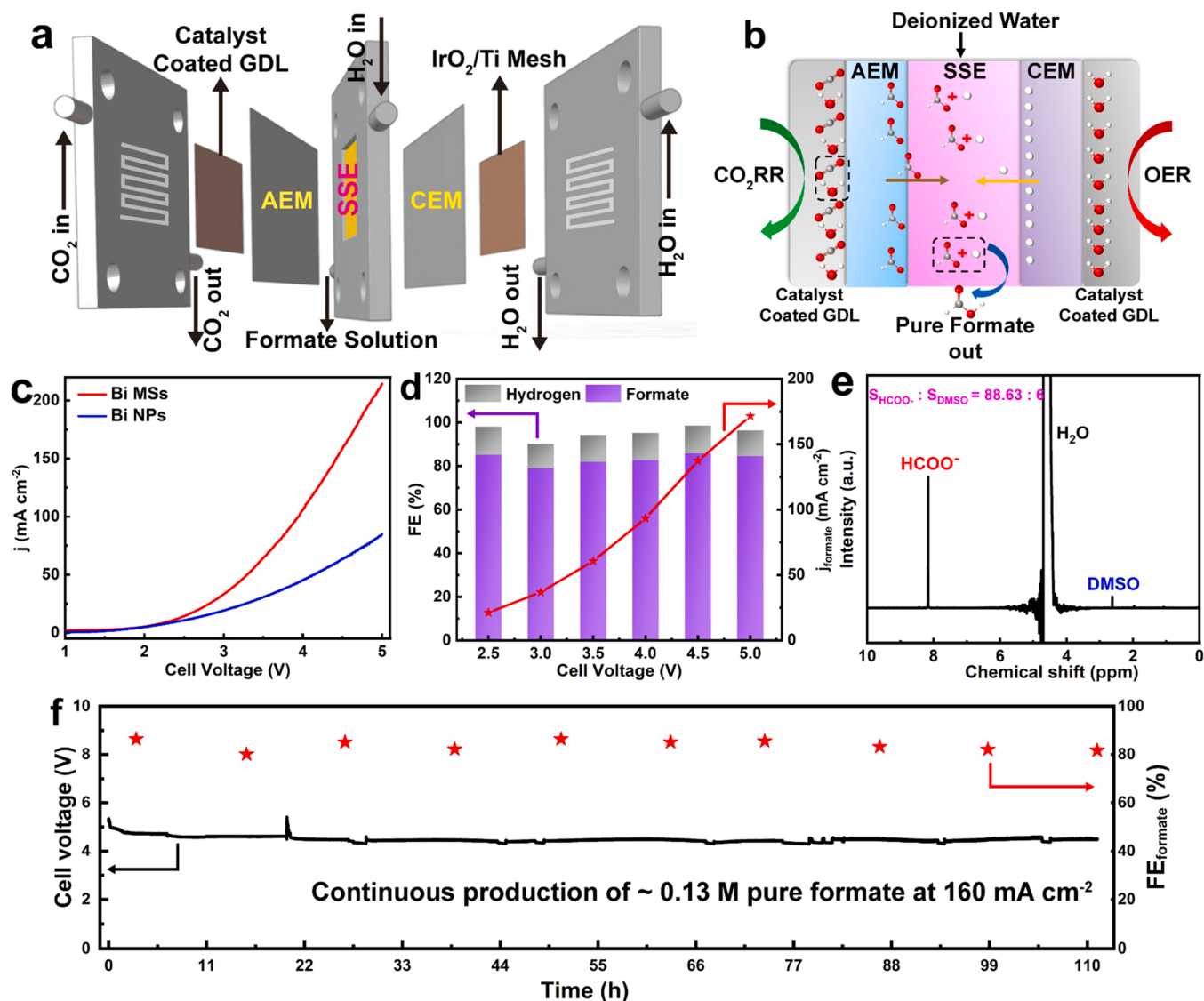


**Fig. 5.** (a) Structure sketch and (b) schematic diagram of the solid-state electrolytic cell. (c) LSV curves of Bi MSs and Bi NPs in the solid-state electrolytic cell. (d) FEs of Bi MSs in the solid-state electrolytic cell at different cell voltages. (e) <sup>1</sup>H NMR spectrum of pure formate solution produced at 4.5 V (diluted to 40 mL with deionized water). (f) Stability test of solid-state electrolytic cell for continuous production of pure formate solution at 160  $\text{mA cm}^{-2}$  for 110 h.

produce higher formate solution concentrations at higher current density and exhibit excellent long-term stability in the solid-state electrolytic cell compared to what has been reported [5,22,30]. In conclusion, the high activity and selectivity of Bi MSs and the application of solid-state electrolytic cell provide prospects for electrocatalytic commercial production of formate.

#### 4. Conclusion

In conclusion, Bi MSs catalyst for the stable and efficient production of formate by ECO<sub>2</sub>RR were in-situ prepared by electroreduction of Bi<sub>4</sub>O<sub>7</sub>. In the H-type electrolytic cell, Bi MSs affords an excellent selectivity (96.20%) for formate generation within a wide potential window, and the stability is maintained for at least 52 h. The enhanced ECO<sub>2</sub>RR performance can be attributed to the excellent intrinsic activity and the formation of abundant three-phase interfaces on the hydrophobic surface of Bi microsheets, which enhances CO<sub>2</sub> mass transfer and suppresses HER. On this basis, Bi MSs enable long-term and direct production of pure formate solutions in a solid-state electrolytic cell. This work provides a convenient and efficient route for the development of high-efficiency electrocatalysts and the production of pure formate solution.

#### CRediT authorship contribution statement

**Yong Zhang:** Investigation, Methodology, Validation, Formal analysis, Data curation, Visualization, Writing – original draft. **Rui Zhang:** Investigation, Formal analysis. **FeiFei Chen:** Investigation, Formal analysis. **FeiFei Zhang:** Formal analysis, Investigation, Resources. **Yingda Liu:** Investigation, Formal analysis. **Xiaoya Hao:** Investigation, Formal analysis. **Haokun Jin:** Investigation, Formal analysis. **Xinghua Zhang:** Formal analysis, Resources. **Zunming Lu:** Formal analysis, Resources. **Hong Dong:** Formal analysis, Investigation. **Feng Lu:** Formal analysis, Investigation. **Weihua Wang:** Formal analysis, Investigation. **Hui Liu:** Formal analysis, Supervision. **Hui Liu:** Formal analysis, Writing – review & editing, Funding acquisition. **Yahui Cheng:** Formal analysis, Project administration, Writing – review & editing, Conceptualization, Funding acquisition.

#### Declaration of Competing Interest

The authors declare that they have no known competing financial interests or personal relationships that could have appeared to influence the work reported in this paper.

## Data Availability

Data will be made available on request.

## Acknowledgements

This work was supported by the following grants: National Natural Science Foundation of China (No. 52071183, 51871122).

## Appendix A. Supporting information

Supplementary data associated with this article can be found in the online version at [doi:10.1016/j.apcatb.2022.122127](https://doi.org/10.1016/j.apcatb.2022.122127).

## References

- [1] J. Wang, H.Y. Tan, Y. Zhu, H. Chu, H.M. Chen, Linking the dynamic chemical state of catalysts with the product profile of electrocatalytic CO<sub>2</sub> reduction, *Angew. Chem. Int. Ed.* 60 (2021) 17254–17267.
- [2] S.C. Lin, C.C. Chang, S.Y. Chiu, H.T. Pai, T.Y. Liao, C.S. Hsu, W.H. Chiang, M. K. Tsai, H.M. Chen, Operando time-resolved X-ray absorption spectroscopy reveals the chemical nature enabling highly selective CO<sub>2</sub> reduction, *Nat. Commun.* 11 (2020) 3525.
- [3] N. Li, P. Yan, Y. Tang, J. Wang, X.-Y. Yu, H.B. Wu, In-situ formation of ligand-stabilized bismuth nanosheets for efficient CO<sub>2</sub> conversion, *Appl. Catal. B* 297 (2021), 120481.
- [4] K. Lei, B. Yu Xia, Electrocatalytic CO<sub>2</sub> reduction: from discrete molecular catalysts to their integrated catalytic materials, *Chem. Eur. J.* 28 (2022), e202200141.
- [5] Z. Wang, Y. Zhou, D. Liu, R. Qi, C. Xia, M. Li, B. You, B.Y. Xia, Carbon-confined indium oxides for efficient carbon dioxide reduction in a solid-State electrolyte flow cell, *Angew. Chem. Int. Ed.* (2022), e202200552.
- [6] T. Zheng, C. Liu, C. Guo, M. Zhang, X. Li, Q. Jiang, W. Xue, H. Li, A. Li, C.W. Pao, J. Xiao, C. Xia, J. Zeng, Copper-catalysed exclusive CO<sub>2</sub> to pure formic acid conversion via single-atom alloying, *Nat. Nanotechnol.* 16 (2021) 1386–1393.
- [7] Y. Xing, X. Kong, X. Guo, Y. Liu, Q. Li, Y. Zhang, Y. Sheng, X. Yang, Z. Geng, J. Zeng, Bi@Sr core-shell structure with compressive strain boosts the electroreduction of CO<sub>2</sub> into formic acid, *Adv. Sci.* 7 (2020), 1902989.
- [8] X. An, S. Li, X. Hao, Z. Xie, X. Du, Z. Wang, X. Hao, A. Abudula, G. Guan, Common strategies for improving the performances of tin and bismuth-based catalysts in the electrocatalytic reduction of CO<sub>2</sub> to formic acid/bismate, *Sust. Energ. Rev.* 143 (2021), 110952.
- [9] X. Zhang, X. Sun, S.-X. Guo, A.M. Bond, J. Zhang, Formation of lattice-dislocated bismuth nanowires on copper foam for enhanced electrocatalytic CO<sub>2</sub> reduction at low overpotential, *Energy Environ. Sci.* 12 (2019) 1334–1340.
- [10] O.S. Bushuyev, P. De Luna, C.T. Dinh, L. Tao, G. Saur, J. van de Lagemaat, S. O. Kelley, E.H. Sargent, What should we make with CO<sub>2</sub> and how can we make it? *Joule* 2 (2018) 825–832.
- [11] L. Peng, Y. Wang, Y. Wang, N. Xu, W. Lou, P. Liu, D. Cai, H. Huang, J. Qiao, Separated growth of Bi-Cu bimetallic electrocatalysts on defective copper foam for highly converting CO<sub>2</sub> to formate with alkaline anion-exchange membrane beyond KHCO<sub>3</sub> electrolyte, *Appl. Catal. B* 288 (2021), 120003.
- [12] J. Li, J. Li, X. Liu, J. Chen, P. Tian, S. Dai, M. Zhu, Y.-F. Han, Probing the role of surface hydroxyls for Bi, Sn and In catalysts during CO<sub>2</sub> reduction, *Appl. Catal. B* 298 (2021), 120581.
- [13] H. Xie, T. Zhang, R. Xie, Z. Hou, X. Ji, Y. Pang, S. Chen, M.M. Titirici, H. Weng, G. Chai, Facet engineering to regulate surface states of topological crystalline insulator bismuth rhombic dodecahedrons for highly energy efficient electrochemical CO<sub>2</sub> reduction, *Adv. Mater.* 33 (2021), 2008373.
- [14] N. Han, Y. Wang, H. Yang, J. Deng, J. Wu, Y. Li, Y. Li, Ultrathin bismuth nanosheets from in situ topochemical transformation for selective electrocatalytic CO<sub>2</sub> reduction to formate, *Nat. Commun.* 9 (2018) 1320.
- [15] D. Yao, C. Tang, A. Vasileff, X. Zhi, Y. Jiao, S.Z. Qiao, The controllable reconstruction of Bi-MOFs for electrochemical CO<sub>2</sub> reduction through electrolyte and potential mediation, *Angew. Chem. Int. Ed.* 60 (2021) 18178–18184.
- [16] Y. Zhao, X. Liu, Z. Liu, X. Lin, J. Lan, Y. Zhang, Y.R. Lu, M. Peng, T.S. Chan, Y. Tan, Spontaneously Sn-doped Bi/BiO<sub>x</sub> core-shell nanowires toward high-performance CO<sub>2</sub> electroreduction to liquid fuel, *Nano Lett.* 21 (2021) 6907–6913.
- [17] D. Wu, G. Huo, W. Chen, X.-Z. Fu, J.-L. Luo, Boosting formate production at high current density from CO<sub>2</sub> electroreduction on defect-rich hierarchical mesoporous Bi/Bi<sub>2</sub>O<sub>3</sub> junction nanosheets, *Appl. Catal. B* 271 (2020), 118957.
- [18] J.H. Koh, D.H. Won, T. Eom, N.-K. Kim, K.D. Jung, H. Kim, Y.J. Hwang, B.K. Min, Facile CO<sub>2</sub> electro-reduction to formate via oxygen bidentate intermediate stabilized by high-index planes of Bi dendrite catalyst, *ACS Catal.* 7 (2017) 5071–5077.
- [19] X. Wei, W. Zhang, D. Liu, D. Liu, Y. Yan, J. Zhang, Y. Yang, S. Yan, Z. Zou, Bi particles with exposed (012) facet on 3D substrate as highly active and durable electrode for CO<sub>2</sub> reduction to formate, *J. CO<sub>2</sub> Util.* 55 (2022), 101797.
- [20] P.F. Sui, C. Xu, M.N. Zhu, S. Liu, Q. Liu, J.L. Luo, Interface-induced electrocatalytic enhancement of CO<sub>2</sub>-to-formate conversion on heterostructured bismuth-based catalysts, *Small* 18 (2022), 2105682.
- [21] X. Feng, H. Zou, R. Zheng, W. Wei, R. Wang, W. Zou, G. Lim, J. Hong, L. Duan, H. Chen, Bi<sub>2</sub>O<sub>3</sub>/BiO<sub>2</sub> nanoheterojunction for highly efficient electrocatalytic CO<sub>2</sub> reduction to formate, *Nano Lett.* 22 (2022) 1656–1664.
- [22] L. Fan, C. Xia, P. Zhu, Y. Lu, H. Wang, Electrochemical CO<sub>2</sub> reduction to high-concentration pure formic acid solutions in an all-solid-state reactor, *Nat. Commun.* 11 (2020) 3633.
- [23] X. Fu, J. Wang, X. Hu, K. He, Q. Tu, Q. Yue, Y. Kang, Scalable chemical interface confinement reduction BiOBr to bismuth porous nanosheets for electroreduction of carbon dioxide to liquid fuel, *Adv. Funct. Mater.* 32 (2021), 2107182.
- [24] T.H.M. Pham, J. Zhang, M. Li, T.H. Shen, Y. Ko, V. Tileli, W. Luo, A. Züttel, Enhanced electrocatalytic CO<sub>2</sub> reduction to C<sub>2+</sub> products by adjusting the local reaction environment with polymer binders, *Adv. Energy Mater.* 12 (2022), 2103663.
- [25] Y. Zhong, Y. Xu, J. Ma, C. Wang, S. Sheng, C. Cheng, M. Li, L. Han, L. Zhou, Z. Cai, Y. Kuang, Z. Liang, X. Sun, An artificial electrode/electrolyte interface for CO<sub>2</sub> electroreduction by cation surfactant self-assembly, *Angew. Chem. Int. Ed.* 59 (2020) 19095–19101.
- [26] P. Yue, Q. Fu, J. Li, L. Zhang, L. Xing, Z. Kang, Q. Liao, X. Zhu, Triple-phase electrocatalysis for the enhanced CO<sub>2</sub> reduction to HCOOH on a hydrophobic surface, *Chem. Eng. J.* 405 (2021), 126975.
- [27] D. Wakerley, S. Lamaison, F. Ozanam, N. Menguy, D. Mercier, P. Marcus, M. Fontecave, V. Mougel, Bio-inspired hydrophobicity promotes CO<sub>2</sub> reduction on a Cu surface, *Nat. Mater.* 18 (2019) 1222–1227.
- [28] S. Chang, Y. Xuan, J. Duan, K. Zhang, High-performance electroreduction CO<sub>2</sub> to formate at Bi/Nafion interface, *Appl. Catal. B* 306 (2022), 121135.
- [29] C.J. Bondu, M. Graf, A. Goyal, M.T.M. Koper, Suppression of hydrogen evolution in acidic electrolytes by electrochemical CO<sub>2</sub> reduction, *J. Am. Chem. Soc.* 143 (2021) 279–285.
- [30] C. Xia, P. Zhu, Q. Jiang, Y. Pan, W. Liang, E. Stavitski, H.N. Alshareef, H. Wang, Continuous production of pure liquid fuel solutions via electrocatalytic CO<sub>2</sub> reduction using solid-electrolyte devices, *Nat. Energy* 4 (2019) 776–785.
- [31] T. Lv, Z. Cheng, D. Zhang, E. Zhang, Q. Zhao, Y. Liu, L. Jiang, Superhydrophobic surface with shape memory micro/nanostructure and its application in rewritable chip for droplet storage, *ACS Nano* 10 (2016) 9379–9386.
- [32] D. Oner, T.J. McCarthy, Ultrahydrophobic surfaces. Effects of topography length scales on wettability, *Langmuir* 16 (2000) 7777–7782.
- [33] D. Wang, Q. Sun, M.J. Hokkanen, C. Zhang, F.Y. Lin, Q. Liu, S.P. Zhu, T. Zhou, Q. Chang, B. He, Q. Zhou, L. Chen, Z. Wang, R.H.A. Ras, X. Deng, Design of robust superhydrophobic surfaces, *Nature* 582 (2020) 55–59.
- [34] Z. Pan, L. Qian, J. Shen, J. Huang, Y. Guo, Z. Zhang, Construction and application of Z-scheme heterojunction In<sub>2</sub>O<sub>3</sub>/Bi<sub>2</sub>O<sub>7</sub> with effective removal of antibiotic under visible light, *Chem. Eng. J.* 426 (2021), 130385.
- [35] X. Feng, K. Jiang, S. Fan, M.W. Kanan, Grain-boundary-dependent CO<sub>2</sub> electroreduction activity, *J. Am. Chem. Soc.* 137 (2015) 4606–4609.
- [36] R.G. Mariano, K. McKelvey, H.S. White, M.W. Kanan, Selective increase in CO<sub>2</sub> electroreduction activity at grain-boundary surface terminations, *Science* 358 (2017) 1187–1191.
- [37] O. Depablos-Rivera, A. Martínez, S.E. Rodil, Interpretation of the Raman spectra of bismuth oxide thin films presenting different crystallographic phases, *J. Alloy. Compd.* 853 (2021), 157245.
- [38] S. Kim, W.J. Dong, S. Gim, W. Sohn, J.Y. Park, C.J. Yoo, H.W. Jang, J.-L. Lee, Shape-controlled bismuth nanoflakes as highly selective catalysts for electrochemical carbon dioxide reduction to formate, *Nano Energy* 39 (2017) 44–52.
- [39] H. Yang, N. Han, J. Deng, J. Wu, Y. Wang, Y. Hu, P. Ding, Y. Li, Y. Li, J. Lu, Selective CO<sub>2</sub> reduction on 2D mesoporous Bi nanosheets, *Adv. Energy Mater.* 8 (2018), 1801536.
- [40] M. Zhao, Y. Gu, W. Gao, P. Cui, H. Tang, X. Wei, H. Zhu, G. Li, S. Yan, X. Zhang, Z. Zou, Atom vacancies induced electron-rich surface of ultrathin Bi nanosheet for efficient electrochemical CO<sub>2</sub> reduction, *Appl. Catal. B* 266 (2020), 118625.
- [41] R. Kortlever, J. Shen, K.J. Schouten, F. Calle-Vallejo, M.T. Koper, Catalysts and reaction pathways for the electrochemical reduction of carbon dioxide, *J. Phys. Chem. Lett.* 6 (2015) 4073–4082.
- [42] W. Shan, R. Liu, H. Zhao, Z. He, Y. Lai, S. Li, G. He, J. Liu, In situ surface-enhanced Raman spectroscopic evidence on the origin of selectivity in CO<sub>2</sub> electrocatalytic reduction, *ACS Nano* 14 (2020) 11363–11372.
- [43] J.E. Pander, III, M.F. Baruch, A.B. Bocarsly, Probing the mechanism of aqueous CO<sub>2</sub> reduction on post-transition-metal electrodes using ATR-IR spectroelectrochemistry, *ACS Catal.* 6 (2016) 7824–7833.